

See discussions, stats, and author profiles for this publication at: <https://www.researchgate.net/publication/257875722>

# Local Ordering Changes in Pt–Co Nanocatalyst Induced by Fuel Cell 2 Working Conditions

ARTICLE *in* THE JOURNAL OF PHYSICAL CHEMISTRY C · JUNE 2012

Impact Factor: 4.77 · DOI: 10.1021/jp2099569

CITATIONS

10

READS

42

9 AUTHORS, INCLUDING:



**Luca Olivi**

Sincrotrone Trieste S.C.p.A.

77 PUBLICATIONS 1,251 CITATIONS

SEE PROFILE



**Sonia Dsoke**

Zentrum für Sonnenenergie und Wasserstoff...

21 PUBLICATIONS 300 CITATIONS

SEE PROFILE



**Roberto Marassi**

University of Camerino

165 PUBLICATIONS 2,790 CITATIONS

SEE PROFILE



**Andrea Di Cicco**

University of Camerino

205 PUBLICATIONS 3,967 CITATIONS

SEE PROFILE

# Local Ordering Changes in Pt–Co Nanocatalyst Induced by Fuel Cell Working Conditions

Giorgia Greco,<sup>\*,†,⊥</sup> Agnieszka Witkowska,<sup>\*,‡</sup> Marco Minicucci,<sup>†</sup> Luca Olivi,<sup>§</sup> Emiliano Principi,<sup>§</sup> Sonia Dsoke,<sup>||</sup> Arianna Moretti,<sup>||</sup> Roberto Marassi,<sup>||</sup> and Andrea Di Cicco<sup>†,¶</sup>

<sup>†</sup>CNISM, School of Science and Technology, Physics Division, University of Camerino, I-62032 Camerino (MC), Italy

<sup>‡</sup>Department of Solid State Physics, Gdansk University of Technology, Narutowicza 11/12, 80-233 Gdansk, Poland,

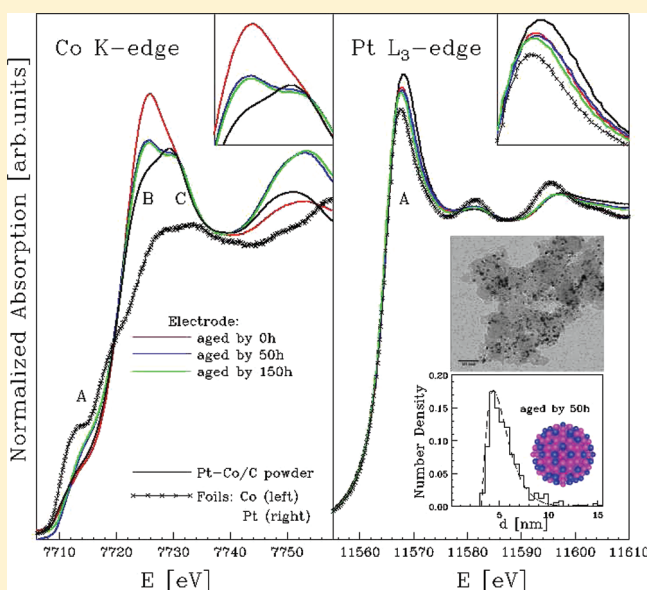
<sup>§</sup>Sincrotrone Trieste ELETTRA, I-34149 Basovizza (Trieste), Italy, and

<sup>||</sup>Department of Chemistry, University of Camerino, I-62032 Camerino (MC), Italy

<sup>⊥</sup>ZSW-Center for Solar Energy and Hydrogen Research, Helmholtzstrasse 8, D-89081 Ulm, Germany

<sup>¶</sup>IMPMC–CNRS, Université Pierre et Marie Curie, 140 rue de Lourmel, F-75015 Paris, France

**ABSTRACT:** We present a detailed investigation of the changes in the local structure and chemical disorder induced by controlled potential cycling in Pt<sub>3±δ</sub>Co nanoparticles used as a catalyst in the proton exchange membrane fuel cell (PEMFC) technology. Various state-of-the-art material science techniques were used to study the microscopic properties of those nanomaterials including ex-situ and in-situ X-ray absorption spectroscopy (XAS), X-ray diffraction (XRD), and transmission electron microscopy (TEM). XAS double-edge multiple-scattering structural refinements of the Pt–Co spectra were performed taking into account the reduction of coordination numbers and degeneracy of three-atom configurations resulting from the measured size distribution obtained by TEM and XRD. The effect of chemical disorder in the considered nanoalloy was also taken into consideration. The PEMFC performance appears to be related to specific changes of the microscopic structural properties of the nanocatalyst during the first operation hours, especially during a cell activation period. In operating PEMFCs a small amount of Co oxide, initially present in the nanoalloy (on the surface of particles), disappeared gradually. At the same time, interatomic Pt–Pt and Pt–Co distances were slightly longer for higher current densities, while distance variances ( $\sigma^2$ ) tended to decrease. Co–Co distribution remained unchanged. By combining XRD and XAS data, we also found that after controlled potential cycling in PEMFC the stoichiometry of the considered alloy changed from the initial Pt<sub>3±δ</sub>Co to Pt<sub>4±δ</sub>Co. Comparison of XAS and XRD-extracted values of the Co atomic fraction indicated that mainly cobalt not fully alloyed with platinum dissolved, and this process occurred in the first degradation period. At the same time, no substantial aggregation processes and no change in the mean size of nanoparticles were observed for this alloy. Accelerated degradation test, lasting up to 150 h, showed structural and electrochemical catalyst stability. The observed increase of chemical and local structural order of the particle core alloy did not affect the ORR kinetics.



## INTRODUCTION

Nowadays the power density requirements for proton exchange membrane fuel cells (PEMFCs) in automotive and stationary applications are within reach. However, successful commercialization of PEMFCs depends on two important issues: fuel cell durability and cost. Therefore, an important field of research is the development of a stable and low-cost electrocatalyst. The performance of fuel cells is usually limited by the slow oxygen reduction reaction (ORR). This obstacle can be overcome using electrodes with a high loading of platinum. However, this

solution is expensive. Binary alloys of various transition metals, such as V, Cr, Co, Ti, and Ni, as well as ternary alloys allow for reduction of the total amount of Pt in a catalytic material and occasionally exhibit even higher ORR electrocatalytic activities than Pt alone.<sup>1–5</sup> Among these, the Pt–Co alloy catalyst seems to be very promising.<sup>1,4</sup>

**Received:** October 17, 2011

**Revised:** May 9, 2012

A major source of catalyst degradation is the loss of electrochemically active surface area (ECSA). In several studies the loss of active platinum by dissolution of Pt was observed.<sup>6–10</sup> Dissolved Pt species can migrate and leave the catalytically active zone (e.g., Pt particles can be detected in the ionomer phase, outside the conductive carbon support<sup>7,8</sup>) or redeposited on other (larger) particles due to their higher equilibrium potential for dissolution (Ostwald ripening).<sup>6,10</sup> There is also evidence for ECSA loss due to other mechanisms, such as agglomeration (due to carbon corrosion or the migration of nanoparticles on the carbon support) and coalescence, which was demonstrated, e.g., in refs 7–14. Attempts to distinguish the relative contribution of each mechanism have also been made,<sup>6,8</sup> but the matter is still under debate. Many works have shown that alloying Pt with transition metals can also improve the stability of the catalyst, particularly those containing cobalt (see, e.g., refs 3, 12, and 13 and references therein).

Several hypotheses have been put forward in the literature to justify the reasons for Pt-based alloys activity and durability increase with respect to pure Pt catalyst. Many experimental and theoretical works show that this enhancement could be attributed mainly to changes in the surface structure and chemical composition of the near-surface region (segregation to the surface and dissolution of atoms and atomic species) and also (as a consequence) in the local geometric structure (i.e., Pt–Pt bond distance, number of Pt nearest neighbors), electronic structure (electron density of states in the Pt 5d band, strength of interaction between the Pt and the 3d transition metal atoms), and nature and coverage of surface oxide layers.<sup>3,4,15–20</sup> However, many of these works considered extended alloy surfaces, and obviously, the mechanisms established for bulk surfaces need not be applicable to nanoparticles. Moreover, often the catalyst was degraded (dealloyed, sintered, annealed, acid treated) in conditions which only mimic the real fuel cell environment.

In this work we focus on the structural changes induced by real fuel cell working conditions observed in a simple bimetallic commercial Pt–Co nanocatalyst supported on Vulcan (E-TEK, 30% of metal and 70% of Vulcan). The structure of the pristine Pt–Co nanomaterial used to prepare the catalytic layers of the studied electrodes was the subject of our previously published work,<sup>21</sup> where a detailed characterization methodology (accounting for size effects and chemical disorder) can be found. The results obtained previously<sup>21</sup> were used as a starting point for the structural analysis presented in this paper.

Understanding the correlation between the changes in the microscopic structure of the catalyst and cell performance is one of the main aims of this work. To achieve this goal, a combination of advanced techniques such as transmission electron microscopy (TEM), X-ray diffraction (XRD), and X-ray absorption spectroscopy (XAS) was applied.<sup>22–25</sup> XAS experiments were performed ex situ (in order to control the changes induced by working time) and in situ (to observe the changes induced by the working potential) using a commercial single PEMFC optimized for XAS measurements and a suitable measurement protocol.<sup>26,27</sup> The obtained high-quality XAS data were used to perform a multiple-scattering (MS) two-edge (Co K and Pt L<sub>3</sub>) analysis employing the GNXAS method.<sup>28,29</sup>

The paper is organized as follows: the subsequent section contains experimental details (i.e., a description of the preparation procedure of the catalytic layer, conditioning of the membrane electrode assembly, and presentation of the

experimental setup). Analysis of the XAS data collected in situ is shown in the section Potential-Dependent Local Structural Changes of the Pt–Co/C Electrocatalyst. The section Durability of Pt–Co/C Electrocatalyst is focused on the structural changes observed in the Pt–Co electrocatalyst subjected to an accelerated degradation test.<sup>13,30</sup> In the final section, we give primary conclusions.

## EXPERIMENTAL DETAILS

**Preparation of the Samples.** In this work we present the analysis of structural changes observed in the commercial catalyst Pt<sub>3±0.6</sub>Co supported on Vulcan (E-TEK product, 30% of metal, and 70% of Vulcan, hereinafter referred to as Pt–Co/C) induced by fuel cell operating conditions. This study was focused on two main aspects of the fuel cell: working potential and working time. In both cases, the studied material was in the form of a thin catalytic layer prepared as follows.

The ink containing the required quantity of the catalytic powder was prepared in a closed glass vial with isopropyl alcohol and a 5% Nafion solution. The dry Nafion content was 35 wt %. The suspension, stirred at room temperature for 24 h, was then brushed on the gas diffusion layer (ELAT GDL, LT1200W, from E-TEK) and dried at 80 °C for 30 min. The total metal loading on the electrode was computed from the weight.

For measurements at variable potential (XAS in-situ experiment) membrane electrode assemblies (MEAs), with an active area of 5 cm<sup>2</sup>, were prepared using Nafion N-117 (DuPont) as a proton conductive membrane, electrode with a Pt–Co/C electrocatalyst (metal loading about 0.1 mg/cm<sup>2</sup>) as a cathode, and electrode with a Pd nanocatalyst supported on Vulcan (E-TEK, metal loading about 1.0 mg/cm<sup>2</sup>) as an anode. The Nafion membrane was sandwiched between these two electrodes, hot-pressed, and positioned between the graphite collector plates of a commercial single fuel cell specifically optimized for in-situ XAS measurements.<sup>26,27</sup> Palladium was used on the anode side, since it is a good catalyst of the hydrogen oxidation reaction and does not disturb X-ray absorption measurements of Pt L<sub>3</sub> and Co K edges.

For the FC working time-dependent study (XAS ex-situ experiment), three electrodes were prepared with a total Pt–Co loading equal to about 1.5 mg/cm<sup>2</sup>. Such electrodes were placed on the cathode side of MEAs (not hot pressed in this case) composed of Nafion N-112R (DuPont) and a Pt standard electrode on the anode side (E-TEK, Pt loading 0.5 mg/cm<sup>2</sup>). Subsequently, MEAs were subjected to the degradation process in a standard single fuel cell. An accelerated test methodology based on a step-like potential cycling<sup>13,30</sup> was applied. The PEMFC was held for 1 h at 0.6 V and 1 h at open-circuit voltage (OCV) for a total time of 0, 50, and 150 h. Each MEA was conditioned in H<sub>2</sub>/O<sub>2</sub> flow on the anode and cathode side, respectively, at 0.6 V for 4 h. The time taken for conditioning did not count toward the working time. Other conditioning and, then, working conditions applied were as follows:  $T_{H_2} = T_{O_2} = T_{cell} = 70$  °C, total pressure  $p_{H_2} = p_{O_2} = 2$  bar, and H<sub>2</sub>/O<sub>2</sub> stoichiometric flow  $s = 1.5/2$  with 100/200 mL/min load based. After the selected working times (0, 50 and 150 h), the electrochemical performance of the cell was checked (see Figure 7), then MEA was dismantled, and the XAS spectra for the Pt–Co/C cathode catalyst under study were collected ex situ.

**TEM and XRD Measurements.** For all considered samples, transmission electron microscopy (TEM) and X-ray diffraction (XRD) pattern measurements were performed to determine the morphology of nanoparticles and their size distribution. TEM images were taken using a JEOL JEM-2100F at Institut de Minéralogie et de Physique des Milieux Condensés, UPMC, Paris, France. On the basis of the profile of randomly selected quasi-spherically shaped particles, we obtained the particle size distribution using the ImageJ program. The particle size distribution is typically asymmetric and exhibits a tail extended to large nanoparticles. Therefore, its shape can be interpolated by an asymmetric  $\Gamma$ -like function

$$f(x) = \frac{2}{\beta\sigma\Gamma(4\beta^{-2})} \left[ 4\beta^{-2} + \left( \frac{2x - 2D_a}{\beta\sigma} \right)^{(4\beta^{-2}-1)} \right] \exp \left[ - \left( 4\beta^{-2} + \frac{2x - 2D_a}{\beta\sigma} \right) \right] \quad (1)$$

where  $D_a$  is the average particle diameter,  $\sigma$  the distribution width, and  $\beta$  the distribution asymmetry parameter.

X-ray diffraction patterns were obtained in reflection mode by a Philips diffractometer (PW1830 X-ray generator) with Bragg–Brentano geometry and Cu  $K\alpha$  radiation ( $\lambda = 1.54178$  Å). A step–scan pattern was collected in the  $1$ – $50^\circ$   $2\theta$  range with a  $0.02^\circ$  step and 3 s per point counting time. The mean Pt–Co crystallite size was estimated by the Scherrer equation<sup>31</sup> from the position and width of the (111), (200), (220), (311), and (222) peaks modeled with a Voigt function. The position of the peaks and fwhm intensities were also used to determine the lattice cell parameter and crystalline phase stoichiometry.

**XAS Measurements.** In order to perform in-situ XAS measurements, an optimized commercial single fuel cell (PEMFC EFC-05-02, Electrochem., Inc.)<sup>26,27</sup> was installed in the X-ray spectrometer BM29 of the ESRF (Grenoble). Optimization consisted in the drilling of a window for the X-ray beam in the shape of a truncated prism. The amount of tested material in the sample was very small (especially in the case of Co, below  $0.01$  mg/cm<sup>2</sup>). For this reason, measurements were performed in fluorescence mode using a 13-channel Ge X-ray detector in the energy range of 11.45–12.3 keV for Pt  $L_3$ -edge and 7.64–8.30 keV for Co K-edge. Prior to collection of XAS spectra, the MEA was conditioned at room temperature (RT) at 0.5 V for 17 h. Afterward, a rapid electrochemical measurement was performed to check the cell performance. The importance of performing a conditioning process, as a part of the MEA activation procedure, is described in the next section Electrolyte Conditioning. XAS data were collected for various cell potentials (from the cathode activation region) at RT under room pressure and with a 100/200 mL/min flow of  $H_2/O_2$  at the anode and cathode side, respectively. A 10 min equilibration was applied to reach a steady state of the catalyst under each of the potential conditions. Acquisition of each spectrum lasted about 60 min.

Ex-situ XAFS measurements were carried out in transmission mode under ambient conditions at the Synchrotron Light Laboratory ELETTRA (Trieste, Italy), 11.1 XAFS beamline, in the energy range of 11.45–12.80 keV for Pt  $L_3$ -edge and 7.60–8.90 keV for Co K-edge. Acquisition of each spectrum lasted about 30 min.

The sampling procedure in fluorescence and transmission modes was chosen so as to yield high-quality data for both pre-

and postedge background analyses used to normalize the spectra. The noise level and quality of the XAS data obtained in situ using the PEMFC XAS setup are also shown and discussed in comparison with standard measurements in refs 26 and 32. Experimental data were analyzed in the near-edge and extended XAFS regions. An advanced technique based on multiple-scattering (MS) theoretical calculations of the X-ray absorption cross-section in the framework of the GNXAS method<sup>28,29</sup> was used for structural refinement. The double-edge MS XAFS analysis methodology applied to account for the reduction of coordination numbers and the degeneracy of three-body configurations related to the mean size of the studied bimetallic particles and also the chemical disorder in the nanoalloy was described in detail in ref 21.

**Electrocatalyst Conditioning.** The electrode preparation procedure is an important step in setting up a fuel cell. It involves not only preparing the ink (mixture of solvent and catalyst) and painting the gas diffusion layer with it but also the initial activation period of the cell. In fact, during the first working hours (i.e., the conditioning period) the electrocatalytic performance of the cell increases and finally becomes stable (see Figure 1). This phenomenon is due to many factors

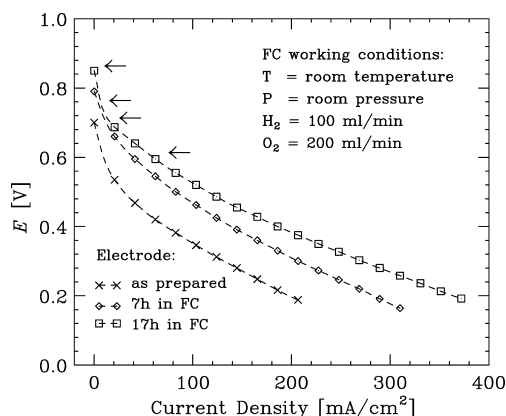


**Figure 1.** Polarization curves obtained at BM29 beamline (ESRF) using Pt–Co/C cathode electrocatalyst during MEA conditioning: as-prepared electrode after 7 and 17 h of FC work. Arrows indicate potential values for which XAFS measurements were performed for the electrode ready to use (see subsequent section).

related, for example, to the humidification of the membrane (dominant factor during the first hour of conditioning), impurity removal (desorption of contaminations originating mainly from the MEA fabrication process, which is the most critical factor affecting FC performance during the first few activation cycles, lasting approximately 7–8 h),<sup>33</sup> and the structural changes in the catalyst. Figure 1 shows that the performance of the cell with the considered Pt–Co/C cathode catalyst after 7 h did not reach the maximum value. It took 17 h of conditioning at RT and 0.5 V to stabilize the performance of the FC. This means that apart from impurity desorption there should be other factors affecting cell performance, e.g., modifications of the structure of the nanoparticles. In order to observe the changes in the structure of the active metal during the activation procedure, XANES and EXAFS results related to three different Pt–Co/C catalytic layer preparation stages were compared: the pristine nanomaterial (in powder form), as-prepared catalytic layer, and conditioned catalytic layer (electrode ready to use).



In Table 1 we report the values of XAS jump (X-ray absorption discontinuity) ratios  $J_{\text{Pt}}/J_{\text{Co}}$  obtained for both the

**Table 1. Values of XAS Jump (X-ray absorption discontinuity) Ratios  $J_{\text{Pt}}/J_{\text{Co}}$  Obtained for Both the Pristine Material and the As-Prepared Electrode<sup>a</sup>**

Pt-Co/C	$J_{\text{Pt}}/J_{\text{Co}}$	Pt:Co(XAS)	Pt:Co(XRD)
powder form	2.95(3)	2.65(2):1	3.08(2):1
as-prepared electrode	3.29(3)	2.80(2):1	3.4(1):1

<sup>a</sup> $J_{\text{Pt}}/J_{\text{Co}}$  is the ratio of the XAS discontinuities (jumps) at the Pt  $L_3$  and Co K edges for the Pt-Co/C powder sample and the as-prepared electrode. The corresponding stoichiometry, Pt:Co(XAS), was compared with the results obtained by XRD pattern analysis, Pt:Co(XRD).

pristine material and the as-prepared electrode. On the basis of these results, alloy stoichiometries were calculated and compared with those obtained by XRD pattern analysis (Table 1). We note an increase in the  $J_{\text{Pt}}/J_{\text{Co}}$  ratio from the pristine material to the as-prepared electrode. This is related to a change in alloy stoichiometry, which can be interpreted as cobalt loss occurring in the first stage of the electrode preparation (this was observed by both XAS and XRD). However, we note that the stoichiometries obtained by XAS (as compared with XRD-extracted ones) indicated a greater amount of cobalt in both stages. This means that some of the Co was not fully alloyed with Pt.

Figure 2 shows the normalized near-edge XAFS spectra of the sample in subsequent preparation stages. The changes in

can also depend on multiple-scattering effects, related to the clearly visible structural changes in the Co neighborhood (compare the spectra of Co hcp foil and Pt-Co/C powder fcc alloy in Figure 2, left). The Pt  $L_3$  peak B (Figure 2, right) provides information about 5d-electron vacancies.<sup>36</sup> An increase in the white-line (WL) intensity is associated with oxidation of the metal. When considering the as-prepared electrode, the Co K-edge exhibits an increase in the oxidation level of Co (an increase in peak B in Figure 2, left), and, following the conditioning period, a reduction in Co oxidation. At the same time, all Pt  $L_3$  near-edge XAFS spectra are rather similar to the spectrum of Pt foil. The intensity of peak B decreases only slightly for subsequent preparation stages. It should be noted that the differences between the powder, as-prepared electrode and the conditioned electrode (ready to use) were not as significantly pronounced for Pt as for Co.

In Figure 3 the Fourier transforms (FTs) of XAFS signals of the sample in subsequent preparation stages are compared,

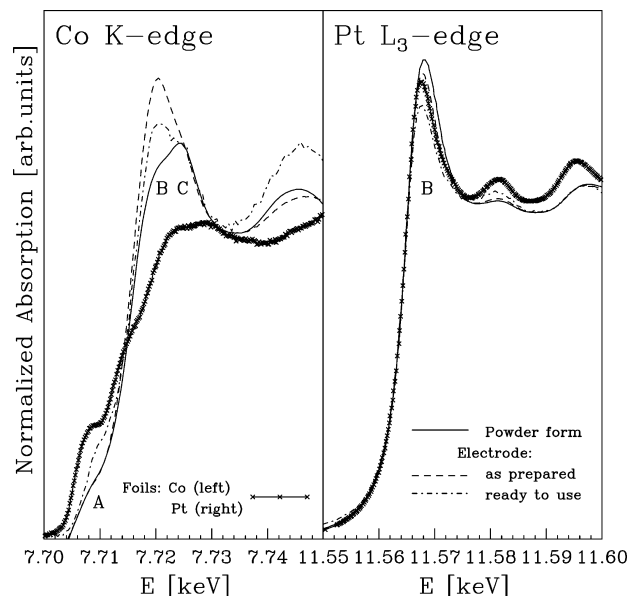


**Figure 2.** Comparison of XANES spectra of the Pt-Co/C catalyst in the powder form, as-prepared electrode (ex-situ measurement), and electrode after conditioning (in-situ blank measurement). Co K-edge (left) and Pt  $L_3$ -edge (right) were also compared with Co and Pt foil spectra, respectively.

the shape and intensity of the features observed near the edge region for both Co K and Pt  $L_3$  edges are clearly visible. The changes in features A, B, and C for the Co K-edge (see Figure 2, left) are mainly related to the variations in the occupancy of the 3d and hybridized 4s, 4p bands, respectively.<sup>34,35</sup> Feature B

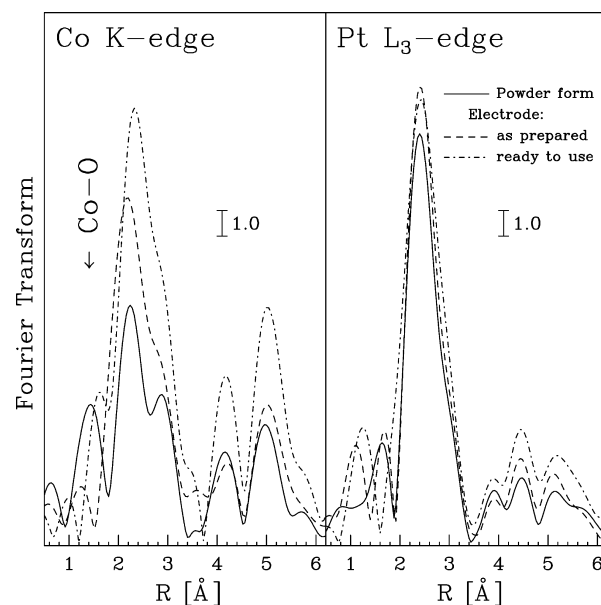


**Figure 3.** Fourier transforms of the XAFS signals of the Pt-Co/C catalyst in the powder form, as-prepared electrode measured ex situ, and electrode after conditioning (ready to use, blank measurements inside the fuel cell): (left) Co K-edge,  $k$  window 3.0–11.3  $\text{\AA}^{-1}$ , weight  $k^3$ ; (right) Pt  $L_3$ -edge,  $k$  window 3.5–11.9  $\text{\AA}^{-1}$ , weight  $k^3$ .

whereas in Table 2 the structural first-shell parameters obtained by XAFS analysis are shown. In the Co K-edge (Figure 3, left) significant changes in the position and intensity of all FT peaks were observed. The intensity changes are a consequence of the ordering process. For the Pt  $L_3$ -edge FTs (Figure 3, right) a modest increase in the intensity was observed, indicating that the ordering process involves mainly the Co sites.

It can be inferred that after the first stage of electrode preparation (catalytic layer preparation), when carbon-supported nanoparticles are mixed with alcohol and liquid Nafion, additional, longer Co–O bonds are formed (the mean bond length increases by about 0.25  $\text{\AA}$ ), and the Co–O distribution exhibits higher structural disorder (as a consequence of impurity generation during MEA preparation). At the same time, the local structure of the nanoparticles of Pt–Co alloy appears to be more ordered, particularly around the cobalt sites.

**Table 2. Structural Parameters Obtained by XAFS Data Analysis for the Pt–Co/C Pristine Material, As-Prepared Electrode (Measured ex Situ), and Electrode after Conditioning (Blank Measurement)<sup>a</sup>**

Pt–Co/C	Pt–Co			Pt–Pt			Co–Co			Co–O		
	R	$\sigma^2$	$N_c$	R	$\sigma^2$	$N_c$	R	$\sigma^2$	$N_c$	R	$\sigma^2$	$N_c$
powder form	2.684(5)	12(1)	3.4(5)	2.703(5)	6.3(8)	7.6(5)	2.689(8)	14(3)	1.1(2)	1.86(1)	2.9(7)	1.1(2)
as-prepared electrode	2.680	9	3.4	2.704	6	7.5	2.689	9	1.1	2.12	6	2.6
electrode ready to use	2.704	7	3.0	2.699	6	8.0	2.690	10	1.7	2.12	2	0.5

<sup>a</sup>R [Å] is the bond distance,  $\sigma^2$  [ $10^{-3}$  Å<sup>2</sup>] is the Debye–Waller-like parameter, and  $N_c$  is the coordination number. Estimated error bars are shown in brackets.

Subsequent preparation stages (conditioning) lead mainly to a decrease in the Co–O coordination number and also to small changes in the Pt–Pt, Pt–Co, and Co–Co coordination numbers (see Table 2). Simultaneously, the Pt–Pt and Co–Co bonds remain unaffected, and only Pt–Co bonds elongate and become more ordered. These changes can be interpreted as a result of Co dissolution and/or a slight increase in chemical disorder.<sup>21</sup> A suitable substitutional disorder parameter (used to describe chemical disorder) for a bimetallic alloy is defined as<sup>21</sup>

$$s = \frac{p - C_a}{1 - C_a} \quad (2)$$

where  $p$  is the probability for selected lattice sites being occupied with atoms M and  $C_a$  is the atomic concentration of the selected chemical species M. Thus,  $s = 0$  indicates random occupancy, and  $s = 1$  indicates perfect chemical order. For nanoalloys, the nanoparticle size and value of the parameter  $s$  determine the coordination numbers and multiplicities of the multiple-scattering signals contributing to EXAFS spectra. It was found that individual EXAFS signals related to the minority species (in this case Co) are extremely sensitive to substitutional disorder, and thus, their intensities, particularly those with collinear three-atom configurations, can be used as a good indicator of the degree of ordering. Taking this effect into account, chemical disorder was estimated on the basis of EXAFS-extracted coordination numbers for the conditioned electrode. The obtained value of  $s$  was equal to 0.5 and only slightly lower than that of the pristine powder ( $s = 0.6$ ).

In conclusion, we attribute the changes in the XAFS signals to be mainly related to the presence of a surface oxide (contamination originating from the MEA fabrication procedure). Oxygen was preferentially bound to cobalt. The Pt–O contribution to the total XAFS signal was always below the measurement sensitivity. The platinum active sites remained almost clean, as also hinted by theoretical simulation.<sup>37</sup> Therefore, the subsequent in-situ measurements of the Pt  $L_3$ -edge were analyzed taking into account Pt–Pt and Pt–Co contributions only. Moreover, during conditioning, Co surface atoms (bonded to O and not fully alloyed with Pt) probably dissolved, the particle surface became more disordered (surface roughening) and clean (absence of cobalt oxide), and the local structure in the core of the nanoparticle became more ordered, leading to an increase in and stabilization of the electrochemical performance, as shown in Figure 1 (in agreement with refs 17 and 38). Consequently, the core–shell particles with thin Pt-rich shell and core with lower Co contents with respect to fresh Pt–Co/C catalyst appeared.<sup>17–19</sup> The results indicate that MEA conditioning, as a crucial process for obtaining a suitable initial cell performance, also results (in the case of nanoalloys) in preparation of catalytic centers at the atomic level, i.e., of the surface of metallic nanoparticles.

**Potential-Dependent Local Structural Changes of the Pt–Co/C Electrocatalyst.** This section is devoted to XAS analysis of the Pt–Co/C catalyst working in the fuel cell under various potentials. Several XAFS spectra were recorded in order to study whether and to what extent the potential losses observed in the cathode activation region are related to the atomic-scale structural changes in the nanocatalyst. The sample used in this experiment was a conditioned (ready to use) electrode, described in the previous section.

Figure 1 shows a typical polarization curve obtained during an in-situ XAS experiment carried out at room temperature. The arrows indicate the potential values for which XAFS spectra were collected. In a kinetically controlled region where XAS measurements were performed, this curve did not differ appreciably from the polarization curve obtained under electrochemically optimized conditions.<sup>39</sup> Measurements for cell potentials below 0.6 V were not carried out for two reasons: (i) on the cathode side the main potential loss (300–400 mV) was observed at low current densities (due to slow electrochemical kinetics); (ii) at lower potentials (higher current densities) the ORR kinetics and, consequently, water production were so high that the water flow through the channels affected the XAFS signal.

Figure 4 shows near-edge XAFS signals for the electrode at various FC working potentials. At open-circuit voltage (OCV  $\approx$  0.85 V) slight oxidation of cobalt was observed (cobalt was still present on the surface of particles). As the voltage was

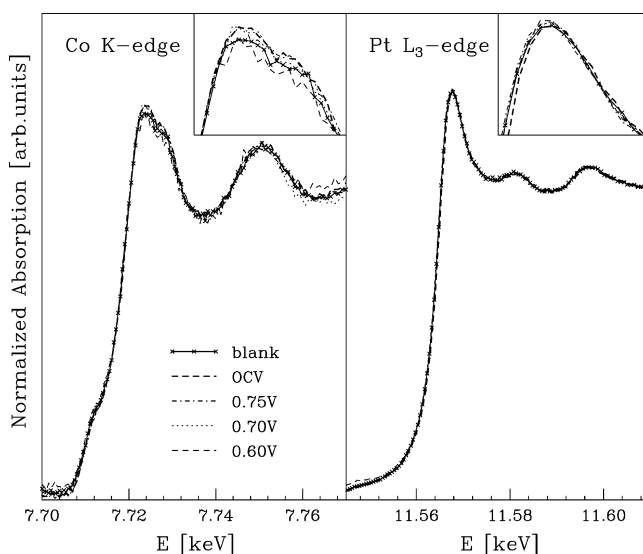


**Figure 4.** Near-edge XAFS spectra of the ready-to-use electrode working in a cell: without gas flux (blank measurement), with gas flux at open-circuit voltage (OCV) and at 0.75, 0.70, and 0.60 V for the Co K-edge (left) and the Pt  $L_3$ -edge (right).

decreased to 0.6 V, a subsequent intensity decrease of the Co K white line occurred. This range of potentials did not correspond to the standard reduction conditions of cobalt, indicating that a certain amount of cobalt oxide may have been dissolved and removed from the nanoparticles surface.

Fourier transforms of  $\chi(k)$  signals collected under various FC conditions for both the Co K and the Pt L<sub>3</sub>-edges are shown in Figure 5. The main results of the XAFS analysis (structural

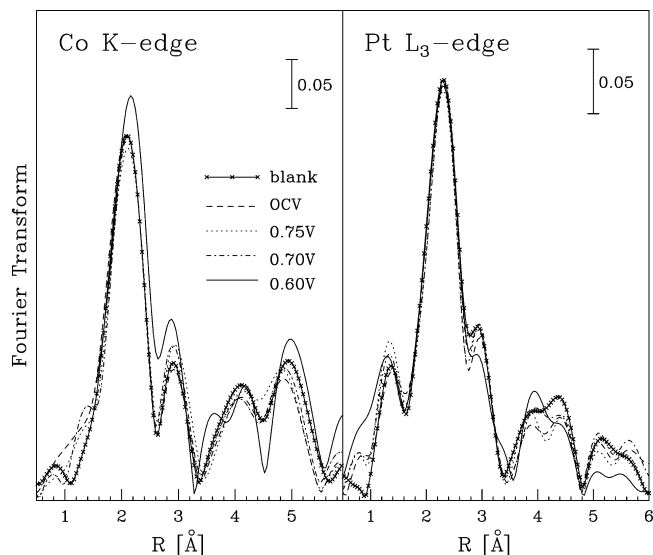
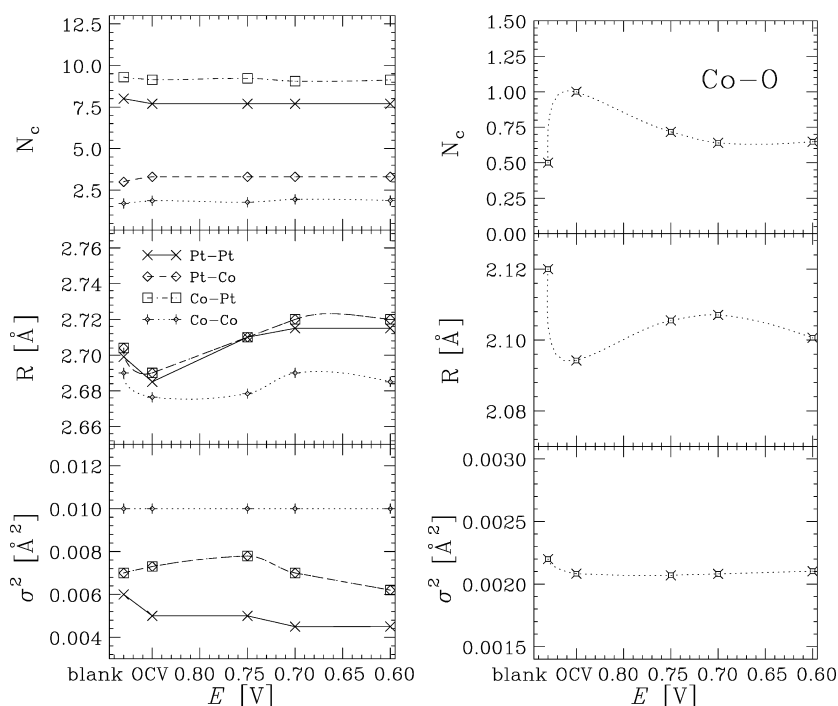


**Figure 5.** Fourier transforms of experimental XAFS signals collected at various FC potentials: cell without gas flux (blank measurement), cell with gas flux at OCV and 0.75, 0.70, and 0.60 V: (left) Co K-edge,  $k$  window 1.9–10.0 Å<sup>-1</sup>, weight  $k^1$ ; (right) Pt L<sub>3</sub>-edge,  $k$  window 3.1–9.4 Å<sup>-1</sup>, weight  $k^1$ .

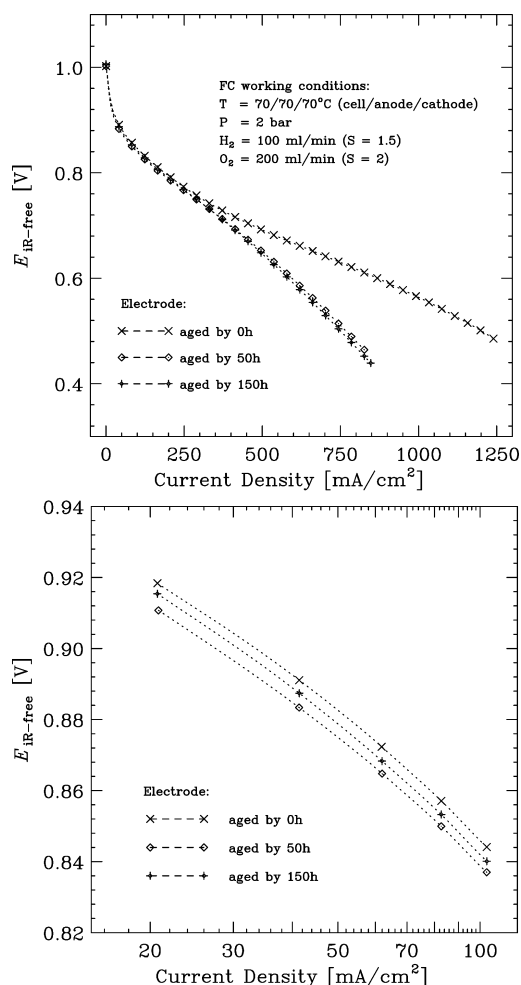
parameters describing first-shell configurations) as a function of the working potential are presented in Figure 6. As evidenced in the figure, the variation in the working potential did not induce visible changes in the coordination numbers ( $N_c$ ) of Pt–Pt, Pt–Co, Co–Pt, and Co–Co configurations, i.e., the chemical order of the nanoalloy was unchanged. Trends for first-shell bond distances ( $R$ ) and structural disorder ( $\sigma^2$ , Debye–Waller-like) parameters of these two-body configurations are also shown in Figure 6 (left). The variation in the parameters describing the Co–O distribution is presented in Figure 6 (right).

Figure 6 demonstrates that subtle changes in the local structure taking place just after the opening of gas flow (OCV conditions). In particular, a slight decrease (about 0.02 Å) in the Pt–Pt, Pt–Co, and Co–O distances and an increase in the Co–O coordination number should be noted. As the working potential is decreased from OCV  $\approx$  0.85 to 0.6 V, the mean Pt–Pt and Pt–Co distances increase by up to 0.03 Å and the Co–O coordination numbers decrease. These results show that the local structure around Co is primarily affected by the operating cell conditions. This particularly concerns Co sites in Co–Pt bonds (Co–Co distribution remains unchanged). This is in agreement with computer simulations,<sup>37,40</sup> which show that the preferential sites for O<sub>2</sub> chemisorption are the ones where Co is surrounded by Pt neighbors. Moreover, the catalyst tends to reach a more ordered structure for higher current densities (low voltage).

**Durability of Pt–Co/C Electrocatalyst.** In Figure 7 typical polarization curves,  $iR$  free (top) and Tafel plots (bottom) obtained for a Pt–Co/C cathode electrocatalyst at various degradation stages are shown. The ohmic loss, which allows calculation of the  $iR$ -free curve, was measured using the current-interrupt technique. It should be noted that 150 h of electrocatalyst working under potential cycling conditions did not strongly affect the electrochemical performance of the cell



**Figure 6.** In-situ EXAFS first-shell results as a function of cell potential. From the top:  $N_c$ , coordination numbers;  $R$ , bond distances;  $\sigma^2$ , distance variance (Debye–Waller-like) parameters. (Left) Pt–Pt, Pt–Co, Co–Pt, and Co–Co configurations; (right) Co–O configuration.



**Figure 7.** Polarization curves (top) and Tafel plots (bottom) obtained using a Pt–Co/C cathode electrocatalyst at various aging stages. Cell working conditions are shown in the figures.

slope of 88 mV/decade. Both the Tafel slopes and the current densities at 0.9 V were similar with the aging. The main change in the potential–current density relation occurred for potentials below 0.75 V. The performance of the cell decreased substantially after the first 50 h of working and was subsequently stabilized. In fact, at 0.6 V, the current density for degraded catalysts was about  $300 \text{ mA}/\text{cm}^2$  lower than for the as-prepared electrode. Mass transport, connected with the poor water management,<sup>41,42</sup> gives the largest contribution to the cell performance at high current density. The presence of liquid water can restrict the gas access and therefore results in higher mass-transport losses. In general, it is very difficult to maintain the cell in fully saturated but not flooded conditions, especially using (as in this specific case) a single serpentine flow channel.

**Analysis of TEM Images.** Figure 8 shows typical TEM images of a Pt–Co/C cathode catalyst scraped from the electrode at various degradation stages. It should be noted that nearly spherical nanoparticles can be easily separated and are quite homogeneously distributed over the carbon support. Figure 8 also presents the distribution of nanoparticle size for each considered sample. The best-fit curves (dashed lines in Figure 8) were obtained for the average diameter ( $D_{\text{TEM}}^a$ ), width ( $\sigma$ ), and asymmetry parameter ( $\beta$ ) values of  $\Gamma$ -like function shown in Table 3. The tails of each distribution include grains of about 8–15 nm in size, which leads to an apparent shift in the mean size with respect to the most probable one. For this reason, the most probable diameters,  $D_{\text{TEM}}^{\text{mp}}$ , were also presented in Table 3. This table shows that for all the considered samples the nanoparticle mean size is estimated at about 5.4(1) nm, whereas the most probable size is about 4.5(1) nm. Other than that, the size distributions for all examined samples are comparable ( $\sigma \approx 1.3(1)$  nm and  $\beta \approx 1.3(2)$ ). This means that during 150 h of an accelerated degradation test performed with a Pt–Co/C nanocatalyst the granular metallic structure exhibits high stability. Moreover, it should be noted that after 50 h of aging a fraction of small particles (with diameters below 3 nm) disappeared entirely.

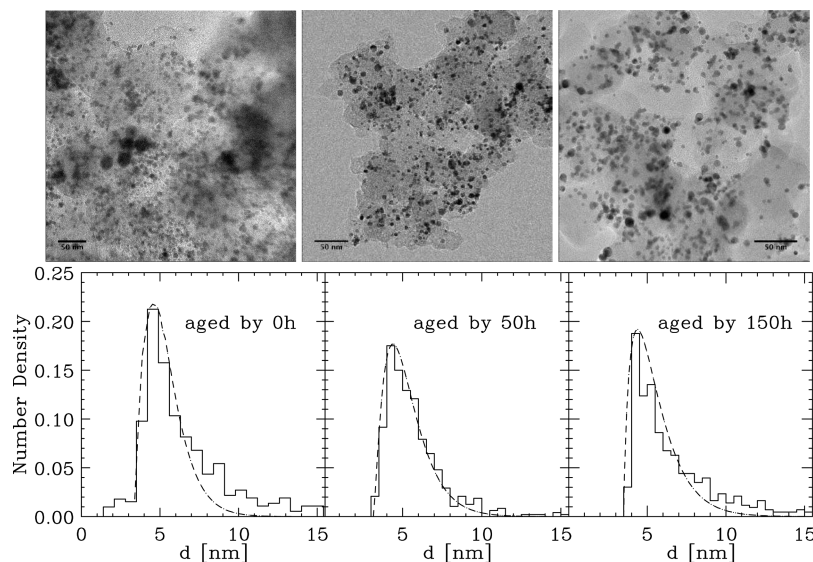


**Figure 8.** TEM images of a Pt–Co/C cathode electrocatalyst (from left to right: electrode after 0, 50, and 150 h of aging), and distribution of nanoparticle size obtained from analysis of TEM images. Dashed lines indicate the best fit to the distribution, obtained with a  $\Gamma$ -like function.



**Table 3.** (Left) Parameters of Size Distributions Obtained by TEM Images Analysis, (Middle) Results Obtained by XRD peak Profile Analysis, and<sup>a</sup> (Right) XAFS Pt L<sub>3</sub>-Edge and Co K-Edge Jump Ratio Used To Calculate Pt:Co Stoichiometry and the Co Atomic Fraction,  $f_{\text{Co}}$

Pt–Co/C electrode	$D_{\text{TEM}}^{\text{a}}$ [nm]	$\sigma$ [nm]	$\beta$	$D_{\text{TEM}}^{\text{mp}}$ [nm]	$D_{\text{XRD}}$ [nm]	$a$ [Å]	Pt:Co	$f_{\text{Co}}$	$J_{\text{Pt}}/J_{\text{Co}}$	Pt:Co	$f_{\text{Co}}$
aged for 0 h	5.4(1)	1.2(1)	1.4(1)	4.5	5.0(5)	3.848(5)	3.5(1):1	0.22(1)	3.298(3)	2.65(4):1	0.27(1)
aged for 50 h	5.3(1)	1.3(1)	1.2(1)	4.5	4.9(5)	3.854(5)	4.0(5):1	0.20(1)	5.064(3)	3.8(1):1	0.21(1)
aged for 150 h	5.4(1)	1.3(1)	1.4(1)	4.5	5.0(5)	3.855(5)	4.0(5):1	0.20(1)	5.204(8)	3.9(1):1	0.20(1)

<sup>a</sup>  $D_{\text{TEM}}^{\text{a}}$ , average diameter;  $\sigma$ , HWHM of the distribution;  $\beta$ , distribution asymmetry parameter;  $D_{\text{TEM}}^{\text{mp}}$ , most probable diameter;  $D_{\text{XRD}}$ , diameter of platinum cobalt nanocrystals;  $a$ , fcc lattice parameter;  $f_{\text{Co}}$ , atomic fraction of Co obtained using values of  $a$  and eq 3.

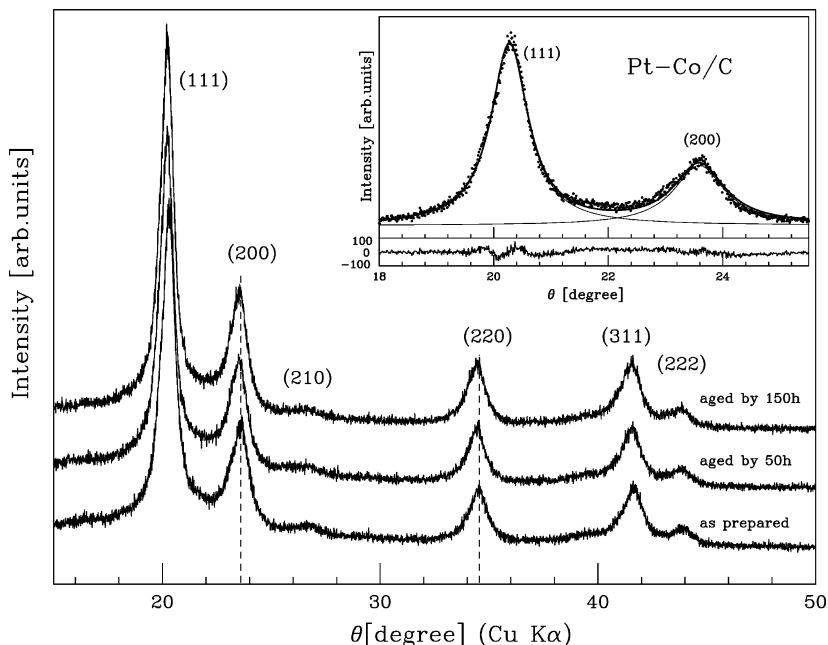


**Figure 9.** Comparison of X-ray reflective diffraction patterns of as-prepared Pt–Co/C cathode electrodes (after 0 h) and after 50 and 150 h of aging. (Inset) Result of analysis of the shape of (111) and (200) peaks obtained for an electrode aged for 0 h; residual curve below the diffraction pattern exhibited good agreement between the experimental (points) and the calculated (solid line) patterns.

**Analysis of XRD Patterns.** Figure 9 presents a comparison between XRD patterns of the Pt–Co/C catalyst at various degradation stages. The structure of the patterns and positions of the peaks indicate that the platinum cobalt nanoparticles are in a single phase with the fcc crystalline structure. No additional well-separated peaks or shoulders were observed. A detailed analysis of the shapes of XRD peaks was performed for all measured samples (see the inset to Figure 9). The obtained particle sizes,  $D_{\text{XRD}}$ , and fcc lattice cell parameter,  $a$ , are shown in Table 3. The diameter of the particles, obtained by averaging of the results over 5 Bragg peaks, was independent of the aging time and equal to  $5.0 \pm 0.5$  nm. Thus, it was in fair agreement with the TEM result. Simultaneously, with an increase in the catalyst working time, we observed a slight increase in the lattice cell constant (about 0.007 Å after 150 h of working). However, it should be underlined that the main change in the value of  $a$  occurred after the first degradation period (50 h). During the subsequent 100 h the value of the fcc lattice cell parameter remained practically unchanged. If we assume that for the considered carbon-supported platinum cobalt alloy the dependence of alloy lattice cell parameter on the content of Co in crystallites follows Vegard's law (as for unsupported platinum cobalt alloys<sup>43,44</sup>), the Co atomic fractions,  $f_{\text{Co}}$ , could be estimated by the relation

$$f_{\text{Co}} = \frac{(a - a_0)}{(a_s - a_0)} f_s \quad (3)$$

where  $a_0$  and  $a_s$  are the lattice parameters of pure Pt (0.3925 nm) and the PtCo alloy (0.375 nm<sup>45</sup>), respectively, and  $f_s = 0.5$  is the atomic fraction of Co in the PtCo alloy. The obtained atomic fractions of Co corresponding to XRD-extracted cell parameters are shown in Table 3. The values of  $f_{\text{Co}}$  were also used to determine the Pt:Co stoichiometry in the nanocrystallites (see Table 3). The results show that the stoichiometry in crystalline nanoparticles of a platinum cobalt alloy for an electrode aged for 0 h was 3.5:1 (rich platinum alloy). After 50 h of working under potential cycling conditions the stoichiometry of the catalytic material reached 4.0:1, with no subsequent variation in the Pt:Co relation observed.

**Analysis of XANES Spectra.** Table 3 shows the ratio of Pt L<sub>3</sub>-edge to Co K-edge jumps ( $J_{\text{Pt}}/J_{\text{Co}}$ ) for each electrode. The XAFS jumps are proportional to the amount of each metal in the sample, and the alloy stoichiometry can be estimated based on this ratio. The Pt:Co stoichiometries obtained in this way are also presented in Table 3. The stoichiometry varied gradually with aging. The biggest difference was observed between the electrodes degraded for 0 h and those degraded for 50 h.

Comparison of normalized XAFS spectra in the near-edge range of Pt–Co/C alloy electrocatalyst at various aging stages is

shown in Figure 10. The reference spectra of Pt–Co/C in powder form and of foils of Co and Pt are also presented in this

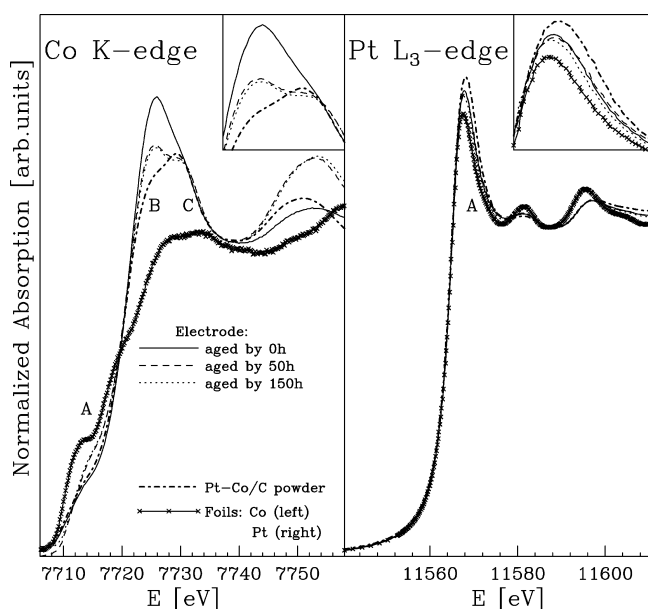


**Figure 10.** Normalized XANES spectra (after background subtraction) of the Pt–Co/C cathode electrocatalyst at various aging stages. Spectra of the Pt–Co/C powder and of Co and Pt foils are also shown for comparison: (left) Co K-edge, (right) Pt L<sub>3</sub>-edge.

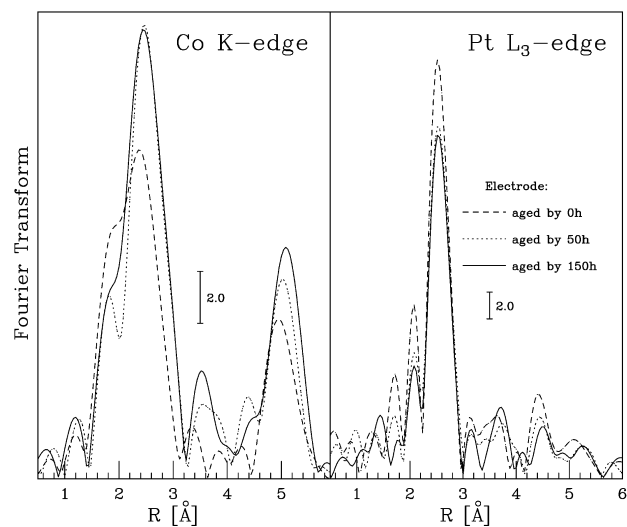
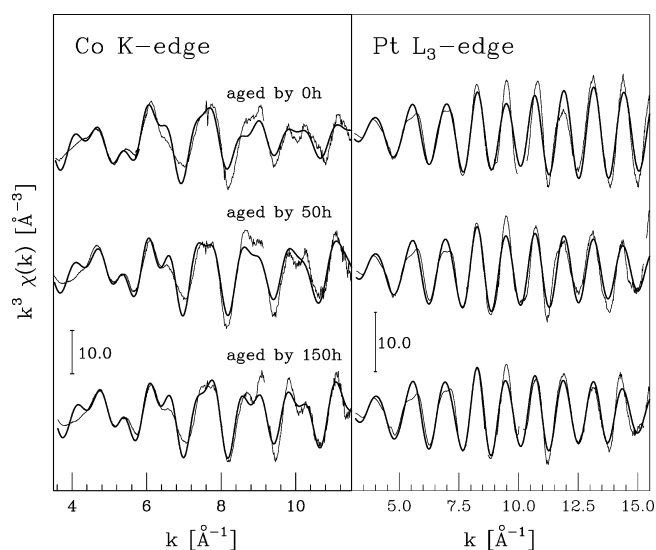


**Figure 11.** XAFS signals (top) and their Fourier transforms (bottom) of the Pt–Co/C cathode electrocatalyst at various aging stages: (left) Co K-edge,  $k$  window 3.6–12.4 Å<sup>−1</sup>, weight  $k^3$ ; (right) Pt L<sub>3</sub>-edge,  $k$  window 3.2–16.0 Å<sup>−1</sup>, weight  $k^3$ .

The intensity of the first FT peak of the Co K-edge (corresponding to the nearest neighbors of Co) already increased strongly after 50 h of aging (Figure 11, left). The increase of the magnitude of the peaks corresponding to distant neighbors was more gradual.

At the same time, the Pt L<sub>3</sub>-edge FTs (Figure 11, right) showed a rather different behavior. A pronounced decrease in the intensity of the first peak (nearest neighbors of Pt) was observed after 50 h of aging, and then after the subsequent 100 h, only a slight change took place. Detailed analysis of these structural changes as a function of aging time was performed using double-edge MS XAFS refinement (GNXAS<sup>21,28,29</sup>). In the analysis, we took into account the effect of coordination numbers and three-atom configurations degeneracy reductions due to the nanometric size of the particles as determined by XRD and TEM analysis (see also previous works<sup>21,32</sup>). In this approach, among other things, the total first-shell coordination number (total number of Co–Pt and Co–Co neighbors at Co sites and of Pt–Pt and Pt–Co neighbors at Pt sites) was constrained to 11.0 for our catalysts, whose average particle

**Analysis of XAFS Spectra.** The XAFS signals and their Fourier transforms are reported and compared in Figure 11.

**Table 4. First-Shell Structural Parameters Obtained by GNXAS Analysis for Pt–Co/C Nanocatalyst Aged for Various Times<sup>a</sup>**

Pt–Co/C electrode	Pt–Co			Pt–Pt			Co–Co			Co–Pt			Co–O		
	R	$\sigma^2$	$N_c$	R	$\sigma^2$	$N_c$	R	$\sigma^2$	$N_c$	R	$\sigma^2$	$N_c$	R	$\sigma^2$	$N_c$
aged for 0 h	2.68	9	3.4	2.70	6	7.5	2.69	9	1.1	2.68	9	9.9	2.12	6	2.6
aged for 50 h	2.70	8	3.3	2.72	7	7.7	2.66	10	0.7	2.70	8	10.3	2.12	8	0.7
aged for 150 h	2.70	8	3.3	2.72	8	7.7	2.66	10	0.7	2.70	8	10.3	2.09	2	0.2

<sup>a</sup>R [Å] is the mean bond length,  $\sigma^2$  [10<sup>−3</sup> Å<sup>2</sup>] is the Debye–Waller-like parameter, and  $N_c$  is the coordination number.

dimension was ca. 5 nm, independently of the working time. The results of XAFS analysis are presented in Table 4. The major changes in the structural parameters took place during the first 50 h of the electrode work. We observed a slight increase in the first-shell Pt–Pt and Pt–Co distances (about 0.02 Å), compatible with the change in the alloy stoichiometry observed by XRD and XANES (an increase in the relative content of platinum). The opposite was observed in the case of the Co–Co distribution: the Co–Co distance became shorter. Local order around Pt and Co atoms, measured by the  $\sigma^2$  parameter, increased for the Pt–Co distributions (distance distribution became narrower) and decreased for the Pt–Pt and Co–Co configurations. Additionally, the amount of Co–O decreased sharply with aging time (after 150 h of working time, the Co–O coordination number decreased to a negligible value, see Table 4). This result corresponds to a decrease in the intensity of peak B observed in the Co K-edge XANES spectra. Moreover, XAFS data analysis offers a possibility to observe the impact of aging on the chemical order in nanoalloys. By looking at the individual coordination numbers reported in Table 4 and calculating the order parameter  $s$  (see ref 21), we can monitor the variation of substitutional disorder as a function of aging time. After 50 h of accelerated degradation, an increase in the order parameter  $s$  from about 0.5(1) to about 0.8(1) was observed. During the subsequent hours of aging, the order parameter did not change beyond the uncertainty bounds.

In summary, in the considered nanostructured Pt–Co/C alloy subjected to accelerated degradation, the Pt local neighborhood was very stable, whereas the average local geometric and electronic structures of Co showed a marked change. Considering that the XAFS measurements were performed *ex situ* (not under the catalyst reduction conditions), these changes were directly related to the effect of catalyst degradation. The bulk of the change was observed just after the first degradation period lasted 50 h. An increase in the atomic Pt:Co ratio (see Table 3) means that over 6% of the total amount of cobalt was lost when the electrocatalyst was working. On the other hand, the fraction of cobalt which was well alloyed with platinum (as evidenced by XRD data) decreased only by about 2%, and consequently, catalyst stoichiometry after 150 h of degradation analyzed by XAFS and XRD reached the same value. At the same time, XRD patterns revealed the absence of pure crystalline Co and crystalline cobalt oxide, the mean particle size remained almost unchanged (see Table 3), chemical order in the nanoalloy increased, Pt–Co distributions became more ordered, and the Co–O contribution almost completely disappeared. These results indicate that loss of Co was mainly associated with dissolution of cobalt which was not fully alloyed with platinum and a large amount of which was in the oxidized form (see, e.g., refs 18, 44, and 46). Hence, cobalt oxide could be present only on the surface of particles; we presume that the core–shell structure with a thin Pt shell was formed during the first hours

of operation of the Pt–Co/C nanocatalyst,<sup>17,46</sup> and subsequent hours in a fuel cell under step-like potential cycling resulted in a more stable Pt skin and more ordered Pt<sub>4±0</sub>Co particles core. Then, until the 150 h of FC operation, the considered Pt–Co/C catalyst exhibited high structural and electrochemical stability. Yu et al.<sup>12</sup> reached a similar conclusion. They reported that the first 400 cycles of square-wave potential cycling between 0.87 and 1.2 V versus RHE (period lasting over 6 h) led to a significant Co dissolution, but then the Pt–Co/C catalyst exhibited high electrochemical stability, up to 40 h of catalyst work. Dubau et al.<sup>19</sup> showed that applying the start/stop degradation procedure in a real FC an even longer period than 150 h is needed to note pronounced Pt–Co/C catalyst ORR activity drop. However, they observed the structural evolution of the nanoparticles toward core–shell structure to compact, spherically shaped “hollow” particles (after over 300 h PEMFC operation) caused by a strong driving force for segregation of Co atoms at the surface. Additionally, Dubau et al. demonstrated that in the long-time operated fuel cell the type of aging protocol and applied potential strongly affect the changes of the nanostructures and, consequently, catalytic activity of the Pt–Co electrocatalysts.

## CONCLUSIONS

This work describes a detailed structural investigation performed for a commercially available Pt-rich Pt–Co alloy nanocatalyst (E-TEK product, 30% of Pt–Co, and 70% of Vulcan). The study is focused on the influence of FC working conditions (cell voltage and cell working time) on the atomic structure, morphology, and chemical disorder in metallic nanoparticles.

XAS measurements performed before and after conditioning demonstrated that the electrochemical performance of a fuel cell can be enhanced by structural modifications occurring at the surface of the metallic nanoparticles. Removal of surface oxide (desorption of the contaminations from MEA preparation procedure) and dissolution of Co surface atoms (leading to higher disorder in the surface of the nanoparticles) were found to be the main nanostructural changes occurring during the cell activation process.

XAFS data of conditioned electrode has shown that cobalt, still present on the surface of the particles, was oxidized right after the opening of the gas flow (OCV conditions). By decreasing the working potential from OCV ≈ 0.85 to 0.6 V, we also detected changes in the Co–O and Co–Pt distributions. In particular, we found that Co sites bound with Pt were most affected by the working conditions (the Co–Co distribution remained unchanged).

The body of the results we obtained suggests that the Pt-rich Pt–Co nanoalloy tested in the present work can be regarded as a good candidate for a stable cathode catalyst. TEM and XRD experiments showed that after 150 h of accelerated degradation test (“step-like” potential variation from OCV to 0.6 V at 70



°C) catalyst nanoparticles did not change their average size and did not form any significant aggregates. Our XAFS and XRD results showed that the stoichiometry of the alloy changed with working time from Pt<sub>3±0</sub>Co to Pt<sub>4±0</sub>Co and, simultaneously, Co–O bonds disappeared. Therefore, loss of Co has been assigned to dissolution of cobalt oxide as a probable effect of the acid environment of the PEMFC. This process appears to involve mainly the non-noble metal oxide, probably originating from the first few monolayers of the alloy surface, and occurs mainly during the first hours of catalyst work. Subsequent hours of operation resulted in a slight increase in structural and chemical local ordering of the nanoparticles which apparently did not affect the FC performance. Consequently, a stable core–shell structure of particles was formed in which no pronounced structural modification was noted after 150 h of work. Much longer test times are thus required to establish precise relationships between the modification of the structural properties of the nanocatalysts and the degradation of the FC electrochemical performance under real working conditions.

## AUTHOR INFORMATION

### Corresponding Author

\*E-mail: giorgiagreco80@gmail.com; agnieszka@mif.pg.gda.pl.

### Notes

The authors declare no competing financial interest.

## ACKNOWLEDGMENTS

We would like to acknowledge J.-M. Guigner who assisted us in the TEM measurements at the Université Pierre et Marie Curie (Paris). We gratefully acknowledge the support of the European Synchrotron Radiation Facility (BM29 station, CH-2879 and CH-2886 proposals) and of the Synchrotron Light Laboratory ELETTRA (XAFS 11.1 station, 2008572 proposal), which provided synchrotron radiation facilities for our experiments. The invaluable help of N. Novello and A. Cognigni during the measurements is also acknowledged. This research was carried out in the framework of the NUME Project “Development of composite proton membranes and of innovative electrode configurations for polymer electrolyte fuel cells” (MIUR, FISIR 2003).

## REFERENCES

- (1) Gasteiger, H. A.; Kocha, S. S.; Sompalli, B.; Wagner, F. T. *Appl. Catal., B* **2005**, *56*, 9–35.
- (2) Wakabayashi, N.; Takeichi, M.; Uchida, H.; Watanabe, M. *J. Phys. Chem. B* **2005**, *109*, 5836–5841.
- (3) Antolini, E.; Salgado, J. R. C.; Gonzalez, E. R. *J. Power Sources* **2006**, *160*, 957–968.
- (4) Stamenkovic, V. R.; Mun, B. S.; Arenz, M.; Mayrhofer, K. J. J.; Lucas, Ch. A.; Wang, G.; Ross, P. N.; Markovic, N. M. *Nat. Mater.* **2007**, *6*, 241–247.
- (5) Dsoke, S.; Moretti, A.; Giuli, G.; Marassi, R. *Int. J. Hydrogen Energy* **2011**, *36*, 8098–8102.
- (6) Ferreira, P. J.; la O', G. J.; Shao-Horn, Y.; Morgan, D.; Makharia, R.; Kocha, S.; Gasteiger, H. A. *J. Electrochem. Soc.* **2005**, *152*, A2256–A2271.
- (7) Xie, J.; Wood, D. L., III; More, K. L.; Atanassov, P.; Borup, R. L. *J. Electrochem. Soc.* **2005**, *152*, A1011–A1020.
- (8) Guilminot, E.; Corcella, A.; Charlot, F.; Maillard, F.; Chatenet, M. *J. Electrochem. Soc.* **2007**, *154*, B96–B105.
- (9) Darling, R. M.; Meyers, J. P. *J. Electrochem. Soc.* **2005**, *152*, A242–A247.
- (10) Virkar, A. V.; Zhou, Y. *J. Electrochem. Soc.* **2007**, *154*, B540–B547.

- (11) Honji, A.; Mori, T.; Tamura, K.; Hishinuma, Y. *J. Electrochem. Soc.* **1988**, *135*, 355–359.
- (12) Yu, P.; Pemberton, M.; Plasse, P. *J. Power Sources* **2005**, *144*, 11–20.
- (13) Borup, R.; Meyers, J.; Pivovar, B.; Kim, Y. S.; Mukundan, R.; Garland, N.; Myers, D.; Wilson, M.; Garzon, F.; Wood, D.; et al. *Chem. Rev.* **2007**, *107*, 3904–3951.
- (14) Kinoshita, K. *Electrochemical Oxygen Technology*; John Wiley and Sons, Inc.: New York, 1992.
- (15) Xiong, L.; Manthiram, A. *J. Electrochem. Soc.* **2005**, *152*, A697–A703.
- (16) Ma, Y.; Balbuena, P. B. *J. Phys. Chem. C* **2008**, *112*, 14520–14528.
- (17) Lai, F.-J.; Su, W.-N.; Sarma, L. S.; Liu, D.-G.; Hsieh, Ch.-A.; Lee, J.-F.; Hwang, B.-J. *Chem.–Eur. J.* **2010**, *16*, 4602–4611.
- (18) Chen, S.; Gasteiger, H. A.; Hayakawa, K.; Tada, T.; Shao-Horn, Y. *J. Electrochem. Soc.* **2010**, *157*, A82–A97.
- (19) Dubau, L.; Durst, J.; Maillard, F.; Guetaz, L.; Chatenet, M.; Andre, J.; Rossinot, E. *Electrochim. Acta* **2011**, *56*, 10658–10667.
- (20) Seminario, J. M.; Agapito, L. A.; Yan, L.; Balbuena, P. B. *Chem. Phys. Lett.* **2005**, *410*, 275–281.
- (21) Greco, G.; Witkowska, A.; Principi, E.; Minicucci, M.; Di Cicco, A. *Phys. Rev. B* **2011**, *83*, 134103–1–134103–10.
- (22) Various authors. In *X-Ray Absorption Fine Structure For Catalysts and Surfaces*; Iwasawa, Y., Ed.; World Scientific: Singapore, 1996; pp 375–384.
- (23) Di Cicco, A.; Berrettoni, M.; Stizza, S.; Bonetti, E.; Cocco, G. *Phys. Rev. B* **1994**, *50*, 12386–12397.
- (24) Boscherini, F.; de Panfilis, S.; Weissmüller, J. *Phys. Rev. B* **1998**, *57*, 3365–3374.
- (25) Frenkel, A. I.; Hills, C. W.; Nuzzo, R. G. *J. Phys. Chem. B* **2001**, *105*, 1115–1118.
- (26) Principi, E.; Di Cicco, A.; Witkowska, A.; Marassi, R. *J. Synchrotron Radiat.* **2007**, *14*, 276–281.
- (27) Principi, E.; Witkowska, A.; Dsoke, S.; Marassi, R.; Di Cicco, A. *Phys. Chem. Chem. Phys.* **2009**, *11*, 9987–9995.
- (28) Filippini, A.; Di Cicco, A.; Natoli, C. R. *Phys. Rev. B* **1995**, *52*, 15122–15134.
- (29) Filippini, A.; Di Cicco, A. *Phys. Rev. B* **1995**, *52*, 15135–15149.
- (30) Zhang, S.; Yuan, X.; Wang, H.; Mrida, W.; Zhu, H.; Shen, J.; Wu, S.; Zhang, J. *Int. J. Hydrogen Energy* **2009**, *34*, 388–404.
- (31) Langford, J. I.; Louër, D.; Scardi, P. *J. Appl. Crystallogr.* **2000**, *33*, 964–974.
- (32) Witkowska, A.; Di Cicco, A.; Principi, E. *Phys. Rev. B* **2007**, *76*, 104110–1–104110–12.
- (33) Jang, J.-M.; Park, G.-G.; Sohn, Y.-J.; Yim, S.-D.; Kim, Ch.-S.; Yang, T.-H. *J. Electrochem. Sci. Technol.* **2011**, *2*, 131–135.
- (34) Hlil, E. K.; Baudoin-Savois, R.; Moraweck, B.; Renouprez, A. *J. Phys. Chem.* **1996**, *100*, 3102–3107.
- (35) Kootte, A.; Haas, C.; de Groot, R. A. *J. Phys.: Condens. Matter* **1991**, *3*, 1133–1152.
- (36) Russell, A. E.; Rose, A. *Chem. Rev.* **2004**, *104*, 4613–4636.
- (37) Balbuena, P. B.; Altomare, D.; Agapito, L.; Seminario, J. M. *J. Phys. Chem. B* **2003**, *107*, 13671–13680.
- (38) Paffett, M.; Beery, J.; Gottesfeld, S. *J. Electrochem. Soc.* **1988**, *135*, 1431–1436.
- (39) Surhone, L.; Timpledon, M.; Marseken, S. *Proton Exchange Membrane*; VDM Verlag Dr. Mueller AG & Co. kg, 2010.
- (40) Balbuena, P. B.; Calvo, S. R.; Lamas, E. J.; Salazar, P. F.; Seminario, J. M. *J. Phys. Chem. B* **2006**, *110*, 17452–17459.
- (41) Pasaogullari, U.; Wang, C. Y. *J. Electrochem. Soc.* **2004**, *151*, A399–A406.
- (42) Yousfi-Steiner, N.; Mocoteguya, Ph.; Candussoc, D.; Hissel, D.; Hernandezb, A.; Aslanides, A. *J. Power Sources* **2008**, *183*, 260–274.
- (43) Denton, A. R.; Ashcroft, N. W. *Phys. Rev. A* **1989**, *39*, 426–429.
- (44) Zignani, S. C.; Antolini, E.; Gonzalez, E. R. *J. Power Sources* **2008**, *182*, 83–90.
- (45) Hansen, J. P.; McDonald, I. R. *Theory of Simple Liquids*; Academic Press: London, 1986.



828 (46) Oezaslan, M.; Heggen, M.; Strasser, P. *J. Am. Chem. Soc.* **2012**,  
829 *134*, 514–524.